Atmospheric Environment 269 (2022) 118854

Contents lists available at ScienceDirect

Atmospheric Environment

journal homepage: www.elsevier.com/locate/atmosenv

Observations of atmospheric oxidation and ozone production in South Korea

William H. Brune [a,*], David O. Miller [a], Alexander B. Thames [a], Alexandra L. Brosius [a], Barbara Barletta [b], Donald R. Blake [b], Nicola J. Blake [b], Gao Chen [c], Yonghoon Choi [c], James H. Crawford [c], Joshua P. Digangi [c], Glenn Diskin [c], Alan Fried [d], Samuel R. Hall [e], Thomas F. Hanisco [f], Greg L. Huey [g], Stacey C. Hughes [b], Michelle Kim [h], Simone Meinardi [b], Denise D. Montzka [e], Sally E. Pusede [i], Jason R. Schroeder [c,1], Alex Teng [h], David J. Tanner [g], Kirk Ullmann [e], James Walega [d], Andrew Weinheimer [e], Armin Wisthaler [j,k], Paul O. Wennberg [h]

[a] Department of Meteorology and Atmospheric Science, Pennsylvania State University, University Park, PA, USA
[b] Department of Chemistry, University of California, Irvine, CA, USA
[c] NASA Langley Research Center, Hampton, VA, USA
[d] Institute of Arctic and Alpine Research, University of Colorado, Boulder, CO, USA
[e] National Center for Atmospheric Research, Boulder, CO, USA
[f] NASA Goddard Space Flight Center, Greenbelt, MD, USA
[g] School of Earth and Atmospheric Sciences, Georgia Institute of Technology, Atlanta, GA, USA
[h] Division of Engineering and Applied Sciences, California Institute of Technology, Pasadena, CA, USA
[i] Department of Environmental Sciences, University of Virginia, Charlottesville, VA, USA
[j] Institute for Ion Physics and Applied Physics, University of Innsbruck, AT, USA
[k] Department of Chemistry, University of Oslo, Oslo, Norway

HIGHLIGHTS

- For South Korea, observed and modeled OH and HO_2 agree to within uncertainties.
- Modeled aerosol uptake of hydroperoxyl is inconsistent with observed hydroperoxyl.
- Missing OH reactivity came from Korea and increased from spring to summer.
- Observed ozone changes are consistent with calculated ozone production.

ARTICLE INFO

Keywords:
Air quality
Hydroxyl
Hydroperoxyl
Aerosol uptake of hydroperoxyl
Missing OH reactivity
Ozone production rate

ABSTRACT

South Korea routinely experiences poor air quality with ozone and small particles exceeding air quality standards. To build a better understanding of this problem, in 2016, the KORea-United States cooperative Air Quality (KORUS-AQ) study collected surface and airborne measurements of many chemical species, including the reactive gases hydroxyl (OH) and hydroperpoxyl (HO_2). Several different results are reported here. First, OH and HO_2 measured on the NASA DC-8 agree to within uncertainties with values calculated by two different box models, both in statistical comparisons and as a function of altitude from the surface to 8 km. These comparisons show substantial scatter, likely due to both variability in instrument performance and the difficulty in interpolating measurements made with frequencies different from those of the model time step. Second, OH and HO_2 calculated by a model including HO_2 uptake on aerosol particles in the chemical mechanism are inconsistent with observations. Third, in the planetary boundary layer over both ocean and land, measured and model-calculated OH reactivity are sometimes different, and this missing OH reactivity, which is as much as ~4 s^{-1}, increased from April to June and originated primarily from the Korean peninsula. Fourth, repeated missed approaches at the Seoul Air Base during several days show that the changes in the sum of ozone and nitrogen

* Corresponding author.
E-mail address: whb2@psu.edu (W.H. Brune).
[1] Now at California Air Resources Board, Sacramento, CA, USA.

https://doi.org/10.1016/j.atmosenv.2021.118854
Received 9 July 2021; Received in revised form 9 November 2021; Accepted 13 November 2021
Available online 20 November 2021

dioxide are consistent with ozone production rates calculated from HO_2 either observed or modeled by the Langley Research Center model.

1. Introduction

South Korea has an air quality problem (Susaya et al., 2013; Jung et al., 2018; Kim and Lee, 2018; Schroeder et al., 2020). While the harmful small particle pollution is easy to see, the harmful ozone pollution lurks unseen. Air quality standards are routinely exceeded in ozone, nitrogen dioxide, and small particles ($PM_{2.5}$), particularly for the Seoul metropolitan area (SMA) (IQAir, 2021). Of the ~52 million South Koreans, about half live in the SMA, which encompasses substantial industrial activity and vehicular traffic. In 2016, over half of freight trucks and almost half of cars used diesel fuel, contributing to the poor air quality in terms of particles and ozone (Reuters, 2021). Since then the proportion of diesel vehicles is beginning to decrease, but air pollution problems remain.

Models used to diagnose air quality contain ozone chemical mechanisms that have been developed over decades and tested against observations in environmental chambers and the atmosphere. The well-known chemistry contained in these models starts with emissions of nitrogen oxides ($NO_x = NO+NO_2$) from combustion and volatile organic compounds (VOCs) from hundreds of sources. The VOCs are initially oxidized by the hydroxyl radical (OH), creating organic peroxyl radicals (RO_2).

These radicals react with nitric oxide (NO) to form nitrogen dioxide (NO_2) and another organic peroxy radical, RO_2. RO_2 can react with NO to form NO_2 and RO, from which O_2 extracts a hydrogen to form the hydroperoxyl radical (HO_2). HO_2 then also reacts with NO to produce NO_2. This NO_2 produced by RO_2 and HO_2 adds to the NO_2 produced in the reaction of NO with O_3. The rapid daytime photo-destruction of NO_2 results in NO and O_3, and within minutes, these reactions set up a balance among O_3, NO_2, and NO (with a small contribution HO_2 and RO_2 in the balance). The new O_3 that is produced by these reactions rapidly partitions between O_3 and NO_2. In addition, any NO_2 produced directly by sources, such as diesel engines, also quickly partitions into NO_2 and O_3. Thus, examining the chemical processes that produce O_3 requires analyzing the changes not in just O_3 but in the sum of O_3 and NO_2, called O_x.

Chemical transport models combine the effects of chemistry and weather in an attempt to simulate observed O_3 in urban and surrounding areas. Many studies show that they can be excellent at simulating average O_3 levels, but they tend to calculate less O_3 at O_3 levels that exceed air quality standards, precisely where their ability to simulate O_3 is needed the most (Appel et al., 2007; Im et al., 2015). Several studies focused on Southeast Asia also find that the models tend to underpredict hazardous O_3 levels (Kang et al., 2016; Oak et al., 2019; Le et al., 2020, Fig. 4; Park et al., 2021). Usually this model failure is attributed to some problem in the model meteorology, emissions inventory, or methodology. Counter to these studies are those involving the weekend-weekday effect, wherein O_3 increases on the weekends when NO_x levels are lower than on weekdays (Harley et al., 2005; Pollack et al., 2013). However, when O_x is considered as opposed to O_3, the recent weekend effect is minimized to just the partitioning between O_3 and NO_2 with NO_x less on weekends so that O_3 is greater (de Foy et al., 2020).

There is a possibility that the well-known O_3 chemistry is incomplete. Most urban measurements of HO_2 show that, for increasing NO, the observed HO_2 becomes increasingly greater than that modeled with a photochemical box model (Brune et al., 2016). Such an increase in HO_2 radicals would lead to more O_3 production than expected at higher NO and could resolve the discrepancy noted in the previous paragraph. Brune et al. suggested the reaction $OH + NO + O_2 \rightarrow HO_2 + NO_2$, but, despite being energetically feasible, it has transition-state energy barriers that prevent it from occurring (Fittschen et al., 2017). Thus, the cause of this widely observed greater-than-expected HO_2 at higher NO amounts remains unresolved.

Aerosol particles can interact with gas-phase reactive gases and solar ultraviolet radiation to alter O_3 production. A recent rise in O_3 pollution in China has been attributed to a decrease in small particles (Li et al., 2018). The chemistry involves the uptake of HO_2 on the particle surfaces, which, depending on the metal content of the particles, will lead to the production of water vapor or hydrogen peroxide (H_2O_2) (Mao et al., 2013). An HO_2 uptake with an effective uptake coefficient of 0.2 in the GEOS-Chem chemical transport model is sufficient to explain the observed O_3 increase over the past four years in China as the aerosol particle amounts have decreased. It is therefore possible that HO_2 uptake on aerosol particles over South Korea is influencing HO_2 and OH just as it appears to be doing over China.

The rich variety of VOCs and high levels of NO and NO_2 emitted in South Korea are combined with the aged pollution coming from China, providing a challenge to model calculations of OH and HO_2. The focus of this paper tests two of model mechanisms using airborne measurements of OH, HO_2, NO, O_3, and ~100 other chemical species during flights over South Korea and its environs in May to June 2016 during the KORea-US cooperative Air Quality (KORUS-AQ) field study (Crawford et al., 2021). Also measured was the OH reactivity, which is the frequency at which the sum of all atmospheric chemical species react with OH. These measurements enable, for the first time, a solid test of model calculations of atmospheric oxidation, including calculated ozone production rates, in South Korea's chemically complex environment.

2. Methods

2.1. KORUS-AQ

KORUS-AQ focused on the air quality of South Korea, with an emphasis on the SMA. The study included enhanced ground sites that complemented the existing National Institute of Environmental Research (NIER) air quality network and four aircraft, including the NASA DC-8. The DC-8 was based in Osan, 47 km south of the center of Seoul. The results of this paper come primarily from measurements made on the NASA DC-8, which conducted 20 flights over, upwind, and downwind of the South Korean peninsula.

The DC-8 carried a suite of instruments that could measure hundreds of chemical species, aerosol properties, photolysis frequencies, and meteorological conditions (Schroeder et al., 2020, Table 2). These measured chemical species include O_3, NO, NO_2, CO, formaldehyde (CH_2O), peroxyacetyl nitrate, and many VOCs, including some C_7 and larger aromatics, and oxygenated VOCs. In addition, the DC-8 also had measurements of the hydroxyl radical (OH), the hydroperoxyl radical (HO_2), and the OH reactivity, which is the inverse of the OH lifetime. This extensive measurement suite enabled comparisons between modeled and measured OH, HO_2, OH reactivity, and calculated net O_3 production rate (PO_3).

A common flight pattern emerged in which the DC-8 would take off from Osan in the morning, and then do an early missed approach at the Seoul Air Base, thus performing an altitude profile through the mixed layer. The Seoul Air Base is located 7 km southeast of the city center. The DC-8 would then execute the rest of the flight pattern for the day, whether it would be upwind or down through flight corridors over South Korea. Often, the DC-8 would execute another missed approach at the Seoul Air Base near midday and then again in the late afternoon near the end of the flight. We call them early, midday, and late throughout the rest of the paper. In this paper, we will use these missed approaches to compare the observed O_x changes to that calculated from the ozone

production rates using the measured and modeled HO_2 and the modeled RO_2.

2.2. OH and HO_2 measurements

OH and HO_2 were both measured using the Penn State Airborne Tropospheric Hydrogen Oxides Sensor (ATHOS) instrument, which uses laser induced fluorescence in low-pressure (3–13 hPa) detection cells to detect OH in one cell and, in a second cell connected to the first, HO_2, which is converted to OH by reaction with NO added between the two cells. ATHOS is discussed extensively in Faloona et al. (2004) and as configured and operated during KORUS in Brune et al. (2020). For KORUS-AQ, OH and HO_2 mixing ratios are reported each 30 s.

The OH signal was separated from background signals by two ways: subtracting the signal when the laser wavelength was not resonant with an OH absorption line from the signal when it is and scrubbing the OH by reacting it with perfluoropropylene in a special inlet attached to the low-pressure detection cell pinhole inlet. For HO_2, the potential interference from some organic peroxy radicals was mitigated by using NO reagent amounts and reactions times so that only ~28% of the HO_2 was converted to OH, a proven method (Fuchs et al., 2011; Feiner et al., 2016). A detailed description of these signal interference reduction strategies is given in Brune et al. (2020).

ATHOS was calibrated in the laboratory and monitors of laser power were used to maintain that calibration during flight. The estimated absolute uncertainty for both OH and HO_2 is ± 35%, 95% confidence. The limit-of-detection (LOD) for OH is set by counting statistics and for HO_2 by small impurities that remained in the reagent NO. For 1-min averages measured in the dark on flights during the NASA Atmospheric Tomography (ATom) mission (Thompson et al., 2021), the standard deviation of the background mixing ratios is 0.018 pptv for OH and 0.2 pptv for HO_2. This standard deviation is taken to be the LOD. In concentration units, the OH LOD is $4.5x10^5$ cm^{-3} at 0 km altitude and $1.5x10^5$ cm^{-3} at 10 km for 1-min averages.

2.3. Measuring atmospheric OH free from interferences

Of the research groups that use LIF to detect OH, we were not the first group to attempt to implement a scrubbing method for OH on an airborne instrument but we were the first to demonstrate this method in a publication (Brune et al., 2020). Some OH interference was measured during KORUS-AQ, but 96% of the statistically significant OH interference (i.e., greater than $5x10^5$ cm^{-3}) was located below 2 km altitude in the planetary boundary layer (PBL). This result is consistent with the results from ATom, which showed no evidence for OH interference above the planetary boundary layer, and for ATom, very little in the PBL. The PBL in KORUS-AQ was more polluted than in ATom, even over the East China Sea, so some OH interference might be expected. On average, only 28% of observed OH below 2 km altitude had statistically significant OH interference and the mean interferences was only 13% of the ambient OH. The OH interference was not observed everywhere, but it was seen in the PBL both over land and ocean.

2.4. OH reactivity measurements

The OH reactivity concept and the basic instrument (Kovacs and Brune, 2001) was redesigned for aircraft operation (Mao et al., 2009), and then further modified for use in KORUS and ATom (Thames et al., 2020). During operation, ambient air flows into a flow tube (15 cm diameter) and past the pinhole inlet to an OH low-pressure detection cell. Clean moist air flows past a mercury lamp in a moveable tube (1.2 cm diameter), producing OH (~10–100 pptv) that is then sprayed into the ambient flow. The OH detection system measures the decay in the OH signal as the moveable tube gets farther from the OH detection system, which increases the reaction time.

The OH reactivity is just the slope of the linear least squares fit to the logarithm of the OH signal versus reaction time when the measured OH loss due to the walls or impurities in clean moist air. A decay was measured every 30 s. The absolute uncertainty due to uncertainties in fitting the linear least squares line to the measured OH signals and in the offset measurement due to wall loss and impurities is estimated to be ± 0.64 s^{-1}, 90% confidence.

This OH reactivity instrument measures the "instantaneous" OH reactivity, which is only the reactions occurring within the measurement time, which is 0.4 s. All subsequent OH reactions with the products of the first OH reaction are typically not measured. However, in environments where NO is greater than a few ppbv, the reaction $HO_2 + NO \rightarrow OH + NO_2$ is fast enough to convert HO_2 to OH, thereby altering the observed OH decay. For the airborne OH reactivity instrument used in KORUS, the analysis program can correct for this recycling from HO_2 to OH for NO amounts only below about ~5–10 ppbv, whereas for the ground-based instrument it is possible to make the correction up for NO as high as 50–100 ppbv. Less than 10% of all OH reactivity measurements were lost by this restriction the data to times when NO was less than 5 ppbv.

2.5. Models

The analysis in the paper uses two different well-established photochemical box models: the NASA Langley Research Center photochemical box model, here called LaRC (Crawford et al., 1999; Olson et al., 2004, 2006; Schroeder et al., 2020), and the F0AM modeling system (Wolfe et al., 2016; Wolfe, 2017) with the Master Chemical Mechanism v3.3.1, here called MCM (Jenkin et al., 2003; Saunders et al., 2003).

Briefly, the LaRC model chemical mechanism has explicit inorganic and reaction rate coefficient for some grouped VOC types. For each 1-s time step along the DC-8 flight path, the model is constrained by the observed chemical species, photolysis frequencies, and meteorological variables and calculates OH, HO_2, some organic peroxyl radicals, and some oxygenated VOCs. It was run so that it achieved diurnal steady-state, that is, the values for these chemical species did not change for the same conditions 24 h later. The model results are archived on a NASA website (Aknan and Chen, 2017). We use the "constrained" runs to better match the constrained input chemical species that we use with the F0AM model framework and MCM.

The MCM model has an explicit mechanism that includes individual chemical species, available measured reaction rate coefficients, available photolysis frequencies, and estimated reaction rate coefficients if measured ones are not available. This mechanism includes several C_{7+} aromatics, which are shown to be important for Seoul (Schroeder et al., 2020). The model was run using the 1-min merge for all flights originating for Osan and again using the 1-s merge for the missed approaches at the Seoul Air Base. It was constrained to all measured chemical species and meteorological conditions in the merges except OH and HO_2, which were calculated.

The model was run repeatedly with different integration and dilution times from hours to days to ensure that the chosen values did produce calculated OH and HO_2 values different from the median values by more than 5%. While OH and HO_2 values were rather immune to the choices of integration and dilution times, the RO_2 values were much more sensitive. For the modeled OH and HO_2 used in this work, the integration and dilution times were both 12 h.

For some MCM model runs, the simplified heterogeneous uptake chemistry for OH and HO_2 described in Brune et al. (2016) was added. This chemistry assumes that only the diffusion to the particles and the surface uptake are important in determining the rate of gas-phase loss and does not consider possible surface photochemistry. The accommodation coefficient, α, was set to 0.2 for both OH and HO_2 (Abbatt et al., 2012), but previous work shows that only the uptake of HO_2 is important because heterogeneous OH uptake is much slower than the gas-phase losses.

In separate model runs, heterogeneous O_3 uptake added to test the

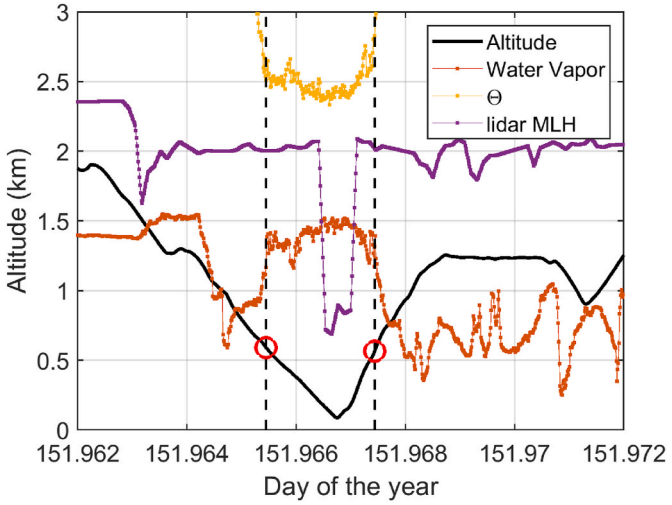

Fig. 1. Method for determining mixed layer height (MLH). Missed approach time series for altitude (black line), scaled water vapor mixing ratio (red line), potential temperature (orange line), and DC-8 lidar determined MLH (purple line). Dashed lines show times when water vapor and potential temperature flatten to within ~10%, indicating a well-mixed mixing layer. The intersection of the altitude and the dashed lines (red circles) are estimates of the MLH. (For interpretation of the references to color in this figure legend, the reader is referred to the Web version of this article.)

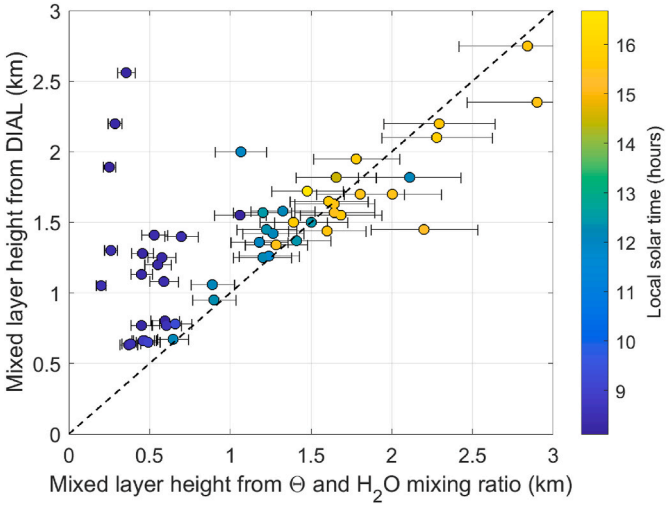

Fig. 2. Estimates of the MLH determined by the flattening of water vapor and potential temperature profiles versus MLH determined from the DC-8 lidar aerosol backscatter. Dot colors indicate time of day. Error bars are estimated uncertainties (30%, 90% confidence) for MLH estimates by the flattening of water vapor and potential temperature. (For interpretation of the references to color in this figure legend, the reader is referred to the Web version of this article.)

possible influence of the heavy aerosol amounts on O_3. The accommodation coefficient was set at 10^{-4}, but it is known to be highly dependent on particle composition and the degree of surface O_3 saturation (Abbatt et al., 2012). The comparisons of the results from these model runs with observations determines the potential for heterogeneous processes to substantially affect fast ozone-producing chemistry.

2.6. Estimating the mixed layer height (MLH)

The mixed layer, or convectively stirred planetary boundary layer (PBL), tends to have fairly constant amounts of aerosol particles, potential temperature, and to a lesser extent water vapor mixing ratio as a function of height. In this paper, three methods are used to determine the MLH: altitude of the enhanced backscattering by aerosol particles of a downward beam from a lidar on the DC-8; altitude at which potential temperature becomes approximately constant to within 10% during a missed approach at Seoul Air Base; and altitude derived by the same approach for water vapor.

A time series of one of the missed approaches demonstrates these methods (Fig. 1). The dashed lines indicate the times for which the water vapor and potential temperature profiles change dramatically. The red circles at the intercept of the dashed lines and the altitude profile indicate the MLH. This method was done subjectively for all of the 53 missed approaches three separate times independently for potential temperature and water vapor and then averaged. The variability in the multiple measurements indicate a typical uncertainty of ± 30%, 90% confidence, in this MLH estimate. The lidar MLH comes from the NASA merge file (Aknan and Chen, 2017).

The MLH from the lidar agrees with that estimated from potential temperature and water vapor for the midday and afternoon missed approaches, but tends to be substantially greater for the morning (Fig. 2). This result should not be surprising because aerosol distributed throughout the higher afternoon mixed layer would remain in the residual layer over night and would give enhanced backscatter starting at the top of the residual layer, not the lower morning mixed layer. Thus, the MLH estimated from potential temperature and water vapor was used in the analysis of O_3 production.

2.7. Analyzing ozone production (PO_3)

The budget equation for O_3 can be written as

$$\frac{\partial O_3}{\partial t} = FO_3 - DO_3 - \frac{v_d O_3}{H} - \boldsymbol{v_H}\cdot\nabla O_3 \qquad \text{(eq. 1)}$$

where $\frac{\partial O_3}{\partial t}$ is the time rate of change for O_3 during the missed approach in ppbv h^{-1}, FO_3 is chemical O_3 production, DO_3 is chemical O_3 loss, $\frac{v_d O_3}{H}$ is surface loss with a deposition velocity v_d and mixed layer height H, and $-\boldsymbol{v_H}\cdot\nabla O_3$ is the horizontal O_3 advection. The net chemical O_3 production is

$$PO_3 = FO_3 - DO_3. \qquad \text{(eq. 2)}$$

And

$$FO_3 = k_{HO2\_NO}[HO_2][NO] + \sum k_{RO2i\_NO}[RO_2]_i[NO] \qquad \text{(eq. 3)}$$

$$DO_3 = k_{O1D\_H2O}\left[O^1(D)\right][H_2O] + k_{O3\_OH}[O_3][OH] + k_{O3\_HO2}[O_3][HO_2] + k_{OH\_NO2}[OH][NO_2] + \sum k_{O3\_VOCi}[O_3][VOC]_i \qquad \text{(eq. 4)}$$

where we have followed the notation in Schroeder et al. (2020). Missing from eq. (1) is the entrainment term for the top of the well-mixed planetary layer, but we will account for the O_3 in the morning residual layer in the analysis.

Because some of the produced O_3 quickly partitions into NO_2 by reaction with NO, the change in $O_x = O_3 + NO_2$ needs to be compared to

PO_3. The missed approaches at the Seoul Air Base three times a day allowed the comparison of the observed O_x change to the calculated O_3 production rate using the measured or modeled HO_2 and the modeled RO_2.

Four estimates of FO_3 come from LaRC HO_2 + LaRC RO_2, MCM HO_2 + MCM RO_2, observed HO_2 + LaRC RO_2, and observed HO_2 + MCM RO_2. The RO_2 values were used as modeled and were not scaled to the differences in observed and modeled HO_2. DO_3 was calculated using LaRC, MCM, and observed OH and HO_2 along with the same other chemical species and reaction rate coefficients. Four PO_3 estimates were found using eq. (2).

Calculated PO_3 averaged for the mixed layer and the residual layer, which is estimated to be the altitudes between the early and late MLHs. The mean PO_3 determined for the column up to the top of the residual layer is the sum of the mixed layer and residual layer PO_3 weighted by the fraction of the column that the two layers occupy. The PO_3 for the late missed approach is unaffected, but the PO_3 for the early missed approach is reduced to 20–25% of the mixed layer value because PO_3 was close to 0 ppbv h^{-1} in the residual layer.

To compare these calculated PO_3 to changes in O_x occurring between early and midday and midday and late, PO_3 was averaged for early to midday and midday to late. The approach outlined below has several assumptions, all with uncertainties. Thus, the best we can expect from this analysis is consistency between observed O_x changes and calculated PO_3 to within an estimated factor of 1.5.

Consider the surface deposition and advection terms in eq (1). At the times of the missed approaches the wind was generally from the west, with a mean direction on 260°, and in the afternoon, the wind speed was typically 5 m s^{-1}. However, O_3 measurements at NIER sites upwind of the Seoul Air Base were generally the same to within less than 20%, implying that advection is not a substantial contributor to $\frac{\partial O_3}{\partial t}$ for the missed approaches at Seoul Air Base. For the surface deposition term, v_d was assumed to be 0.5 cm s^{-1} (Park et al., 2014) and MLH, the mixed layer height, was determined as above. Surface deposition was about 10% of DO_3, the chemical loss.

Two corrections were applied to the observed O_3. First, the ozone in the residual layer became entrained into the mixed layer as the mixed layer grew. Because the midday MLH was fairly comparable with the height of the morning's residual layer, the observed morning O_x was weighted for the amounts of ozone in the mixed layer and the residual layer. Second, in the times between early and midday and midday and late missed approaches, O_3 was lost by chemical reactions, deposition, and, for the test of heterogeneous O_3 loss, heterogeneous reactions. Once these two corrections were made, the corrected O_x from the early missed approach was subtracted from the O_x at the midday missed approach and the corrected O_x from the midday missed approach was subtracted from the O_x at the late missed approach. Each difference was divided by the time between the missed approaches to get an O_x rate-of-change for morning and afternoon.

2.8. Significance of comparisons between observed and modeled OH and HO_2

The uncertainties in the modeled and observed OH and HO_2 affect the assessment of how well the models are representing the oxidation chemistry. In Section 2.3, the estimated absolute uncertainty for the observations is given as ± 35% at 95% confidence, but, for the purposes of this analysis, we will use ± 40% at 95% confidence because it is impossible to account correctly for all contributors to the uncertainty. The modeled uncertainty is estimated from Monte Carlo analyses of a global chemical transport model (Christian et al., 2017) and a photochemical box model (Chen and Brune, 2012; Chen et al., 2012). Typically, these uncertainties ranged from ± 50% to ± 80%, 95% confidence, in the global chemical transport model, although only roughly half was due to photochemistry, and ± 30–± 35%, 95% confidence, in the photochemical box model. As for the observation uncertainty, some modeled uncertainty is likely not included, so we choose a uniform model uncertainty of ± 40%, 95% confidence.

The overlap in the observed and modeled uncertainties is an indicator of the agreement between the observed and modeled OH and HO_2. If values of the observed and modeled OH and HO_2 are separated by ± 40%, with 20% from observed uncertainty and 20% from modeled uncertainty, then the observed and modeled values are different by a confidence interval of 95%, which corresponds to a statistical p-value of 0.05. Thus, if the comparisons of observed and modeled OH and HO_2 disagree by a factor of 1.4, or 40%, then this disagreement is an *indicator* of the transition between agreement and disagreement between observed and modeled OH and HO_2. In scatter plots, we use a York fit (York et al., 2004) because it takes into account the uncertainty of both the observations and the models.

3. Results and discussion

Several results are reported here. First is the comparison between the observed OH and HO_2 and that calculated by the LaRC and MCM models, with the MCM model being run with and without simplified HO_2 heterogeneous uptake. Second is a discussion of heterogeneous uptake of HO_2. Third is the determination of the amount and location of missing OH reactivity in and around the South Korean peninsula. Last is the calculation of PO_3 using measured and calculated HO_2 and OH and the comparison of observed O_3 change rates with those calculated O_3 production rates using observed and modeled HO_2.

3.1. Comparisons of observed and modeled OH and HO_2

Median altitude profiles of OH and HO_2 indicate whether the models are able to simulate OH and HO_2 over a wide range of pressure, environmental factors, and chemical composition (Fig. 3). The two median modeled profiles are in excellent agreement, except for HO_2 in the mixed layer, where LaRC HO_2 is ~30–40% greater than MCM HO_2. Above 3 km, the observed OH and HO_2 are generally 20–50% greater than modeled. As a result, the HO_2/OH ratio modeled by MCM is in excellent agreement with the observed ratio and the LaRC ratio is 10–50% larger at all altitudes. Below 1.5 km altitude, which is the altitude range of greatest interest, the median observed values agree to well within uncertainties with MCM OH and HO_2 and LaRC OH but are ~30% lower than LaRC HO_2, so that the LaRC HO_2/OH ratio is also too large by ~30%.

In regions with sufficient NO, the cycling between OH and HO_2 is substantially faster than HO_x production and loss. Under these conditions, it is easier to diagnose why model OH and HO_2 may be different from observed. In cleaner environments, often HO_x production and loss have rates similar to cycling between OH and HO_2, making it more difficult to diagnose the model-to-observation differences. The differences above 3 km suggest that a HO_x source may be missing in the MCM chemistry because observed OH and HO_2 are both greater than modeled with MCM but the HO_2/OH ratio is the same. Also, these differences suggest that the LaRC chemistry may also have missing OH loss because observed OH is less than modeled but observed and modeled HO_2 agree.

Another way to compare observed and modeled OH and HO_2 is scatter plots (Fig. 4). The slopes for observed versus modeled OH and HO_2 are within 13% of the 1:1 line, indicating that observed OH and HO_2 are not statistically different from modeled OH and HO_2 for both models. The small percent differences of 13% or less confirm this similarity between observations and models. Thus, it appears that both models can generally simulate the observed OH and HO_2.

LaRC and MCM models and their computational strategies are different. First, MCM has fairly explicit oxidation sequences for most of the chemical species measured by the Whole Air Sampler on the NASA DC-8, including the C_{7+} aromatics that were lumped together in LaRC. Second, the approaches to interpolating over gaps between Whole Air

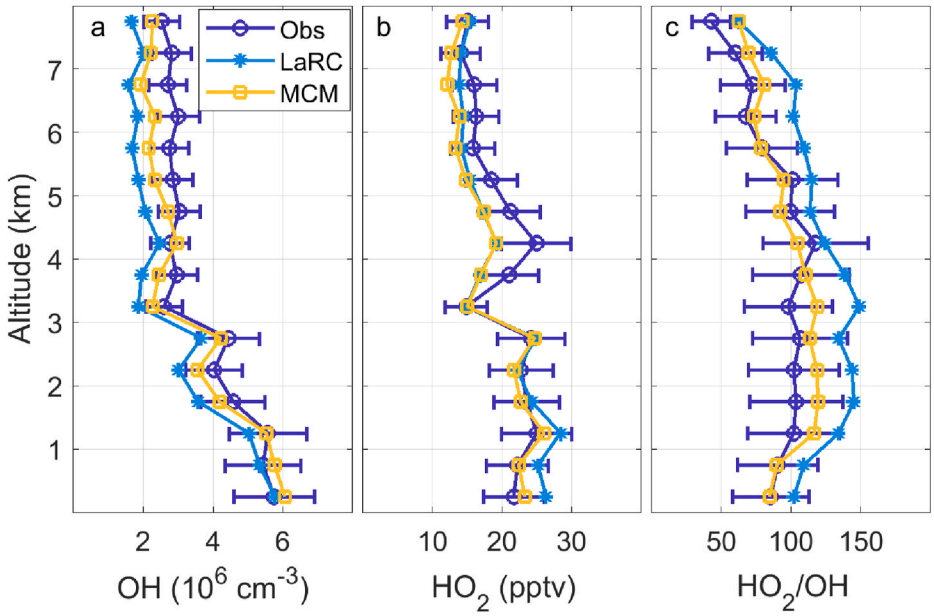

Fig. 3. Altitude profiles for median OH (a), HO_2 (b), and HO_2/OH (c) for observations (blue circles), the LaRC model (light blue stars), and the MCM model (gold squares). Absolute uncertainty (90% confidence) given for observations, and the two models have uncertainties similar to those of the observations. (For interpretation of the references to color in this figure legend, the reader is referred to the Web version of this article.)

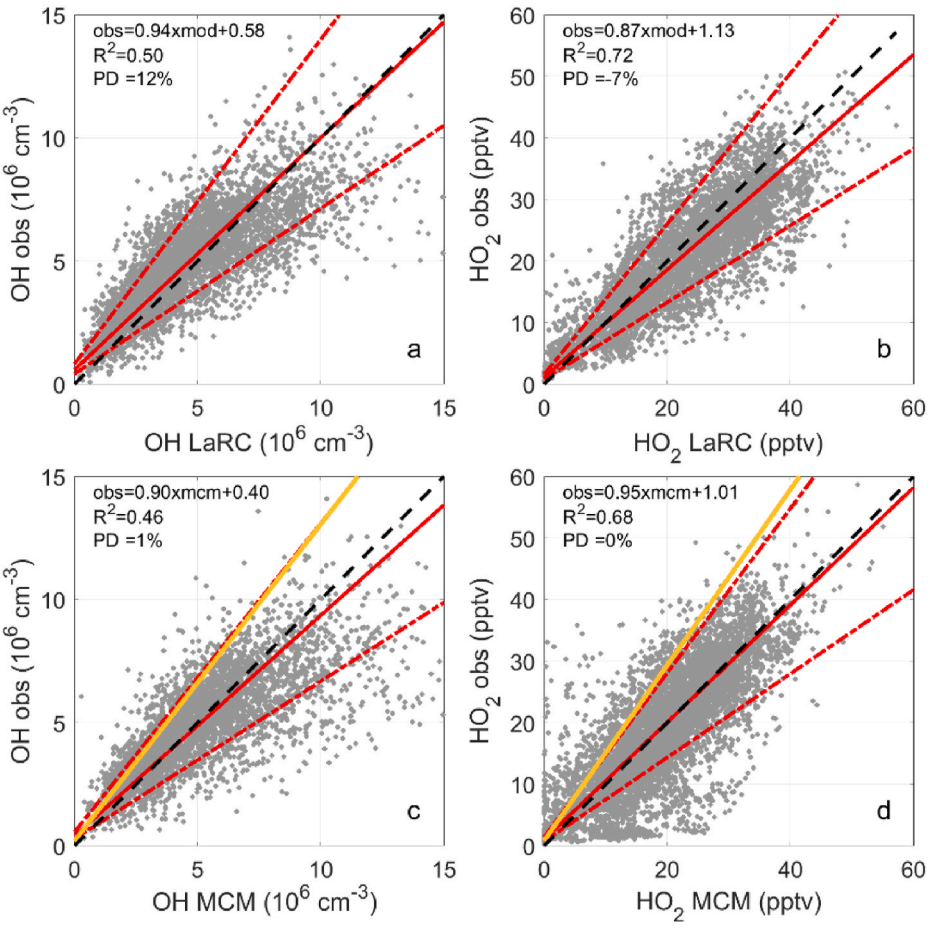

Fig. 4. OH and HO_2: observed versus modeled with the LaRC and MCM mechanisms. Linear fits (red solid lines) and typical combined measurement and model uncertainties (68% confidence level for each), which is a factor of 1.4 (dashed lines), are shown along with the 1:1 line (black dashed line). Also included is the linear fit for the MCM model including heterogeneous HO_2 loss (solid orange line). (For interpretation of the references to color in this figure legend, the reader is referred to the Web version of this article.)

Sampler VOC measurements and missing data for other measurements, while similar, are not the same. Third, MCM is integrated to a fixed period of time, but LaRC is integrated until diurnal steady-state is achieved. Despite these differences, the median observed and modeled OH and HO_2 generally agree to within combined uncertainties for both LaRC and MCM (Fig. 4). The greater apparent scattering for MCM than

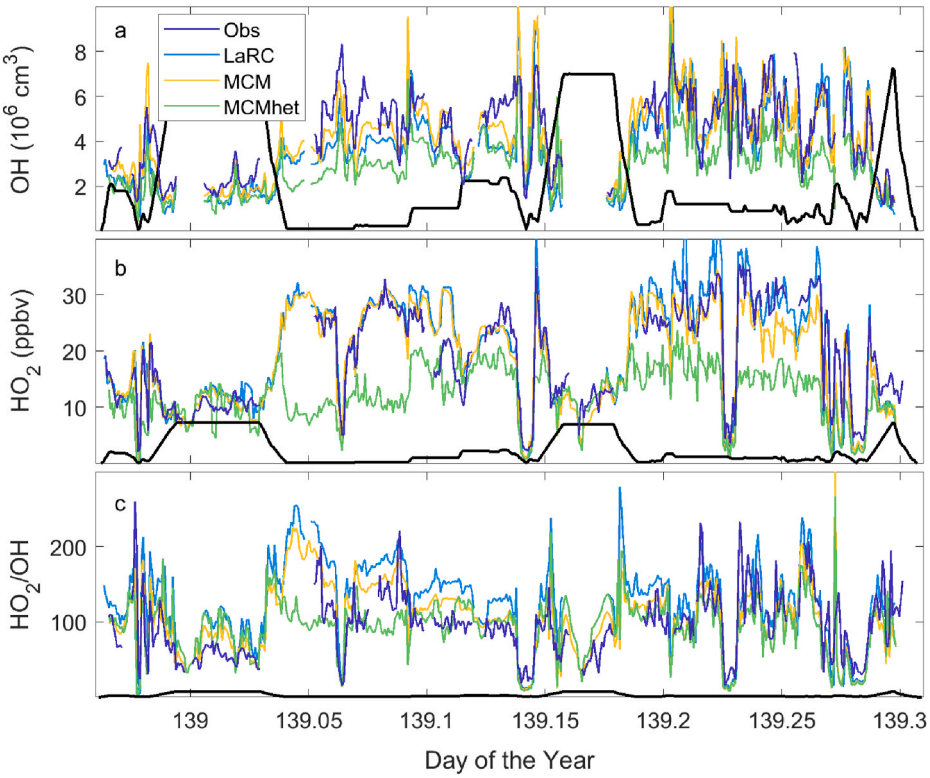

Fig. 5. Time series of OH, HO_2, and HO_2/OH observed (navy lines), modeled with the LaRC mechanism (light blue lines), the MCM mechanism (gold lines), and the MCM mechanism with heterogeneous OH and HO_2 loss (green lines). The altitude in km (black lines) is also shown. The flight was over the East China Sea from 139 to 139.1 and over the Korean peninsula from 139.13 to 139.3. (For interpretation of the references to color in this figure legend, the reader is referred to the Web version of this article.)

LaRC in the HO_2 plot likely results, at least in part, from the sensitivity that these models have to the treatment of the constraining input measurements, including the methods for data gap filling and interpolation from the measurement timestep to the model timestep. This good agreement among modeled and measured OH and HO_2 suggests that model details can be unimportant as long as the chemistry is represented as completely as possible (Schroeder et al., 2020).

However, the observed scatter and the relatively low R^2 values, particularly for OH, indicate that there are significant minute-by-minute differences that the median values and scatter plots gloss over. In Fig. 5, a time series from one flight provides an example of the changes in the relationships of the observed and modeled and even between the two models on relatively short time scales. The substantial differences for OH and HO_2 between the observations and the model including heterogeneous chemistry will be discussed in Section 3.2. For this flight on day-of-the-year (doy) 139 (18 May 2016), the DC-8 took off from Osan, did a missed approach at Seoul Air Base and then a high-level leg over the East China Sea, followed by a low-level-leg return. Then the DC-8 did another missed approach at the Seoul Air Base before a high-level leg over land to Busan, followed by a low-level leg return. Finally the DC-8 did one more missed approach at Seoul Airport before returning to Osan.

The observed to modeled agreement is highly variable, with sudden shifts in agreement with one or both models. For example, over the ocean between for doy between 139.05 and 139.15, OH from observations, LaRC, and MCM are all substantially different even though HO_2 from the three are essentially the same, with the exception of one short period near 139.12. Interestingly, the OH agreement amongst the three is consistently better over land than ocean while the HO_2 agreement is worse.

Variability in the ATHOS calibration is not likely the only explanation for variable agreement between observed and modeled OH and HO_2 because ATHOS calibration shifts on these time scales are typically caused by laser wavelength drift, which affects OH and HO_2 equally, whereas the variations in agreement between models and observations for OH appear to be independent from those in HO_2. In fact, the there is no correlation between the model-observation percent differences for OH and the model-observation percent differences for HO_2 for LaRC ($R^2 = 0.06$) and for MCM ($R^2 = 0.008$). In addition, there is no correlation between the LaRC-MCM percent differences for OH and the LaRC-MCM percent differences for HO_2 ($R^2 = 0.08$). We suggest that these variations in relationships are caused by variations in instrument performance for measurements used to constrain the models and the treatment of constraining observations when interpolating to either a 1-s or a 1-min time interval.

None-the-less, in terms of percent difference, scatter plot slope and intercept, and correlation coefficients, the observed-to-model agreement is about as good as has been obtained on several other airborne missions with ATHOS (Miller and Brune, 2021), particularly those that spent a significant amount of time sampling in the planetary boundary layer.

3.2. *A test of heterogeneous uptake of HO_2 on aerosol particles*

The effects of heterogeneous chemistry involving OH and HO_2 with an accommodation coefficient, α, of 0.2 can been seen in Fig. 4. When diffusion to the surface is considered, the effective uptake coefficient is ~0.17. On the scatter plots, the linear fit to the MCM model with heterogeneous chemistry has a slope of 1.4 for OH and HO_2, just at the edge of being a statistically significant difference. In Fig. 5, the time series shows the effects of heterogeneous chemistry on OH and HO_2 in detail. For the low-level flights over both ocean and land, heterogeneous chemistry reduces modeled OH to ~60% of observed and modeled HO_2 to 35–50% of observed, both substantial amounts.

Another approach to testing whether heterogeneous chemistry is a significant HO_x loss is to plot the ratio of modeled-to-observed OH and HO_2 as a function of aerosol surface area (Fig. 6). Although there is considerable scatter for the individual 1-min data, the median OH and HO_2 modeled-to-observed ratios are both well within uncertainties of 1.0 for more than two decades of aerosol surface area per volume for MCM including only gas-phase chemistry. However, for MCM with heterogeneous chemistry, the modeled-to-observed ratio becomes

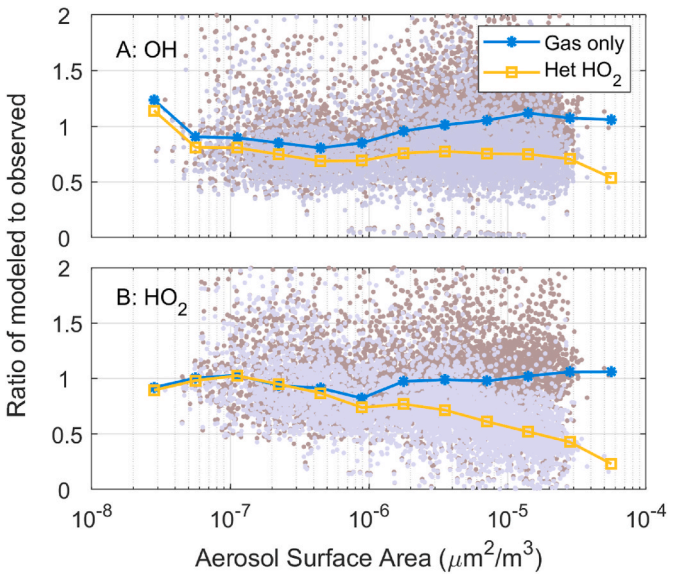

Fig. 6. Modeled-to-observed OH and HO_2 versus aerosol surface area. Plotted are the ratio with the MCM model using only gas-phase chemistry (1-min data points are brown dots; blue linked circles) and the ratio with the MCM model including HO_2 uptake (gray dots; linked golden squares). (For interpretation of the references to color in this figure legend, the reader is referred to the Web version of this article.)

increasingly lower as the aerosol surface area per volume becomes increasingly larger than 10^{-6} μm^2 m^{-3}. At a surface area per volume of 3×10^{-5} μm^2 m^{-3}, the model-to-observed ratio is 0.7 for OH and less than 0.5 for HO_2.

All these different approaches demonstrate that adding HO_2 uptake to the model is inconsistent with the observations for KORUS-AQ. Thus, it is unlikely that O_3 increased in China between 2013 and 2017 because aerosol amount decreased, resulting in less HO_2 uptake, more gas-phase HO_2, and therefore more O_3 production (Li et al., 2018). It is possible that aerosol particles in China have a different chemical composition that those in South Korea. However, a large fraction of aerosol particles in South Korea originate in China (Nault et al., 2018), suggesting that this difference in composition is unlikely to be responsible for substantial differences in HO_2 uptake. This result of little HO_2 uptake is consistent with the results from the Deep Convective Clouds and Chemistry study over the Central United States in summer 2012 (Brune et al., 2018). We therefore conclude that HO_2 uptake on aerosol particles has little, if any, effect on HO_2. More work will be needed to reconcile these results with laboratory studies.

3.3. Missing OH reactivity

Over the past 20 years, ever since we reported the first direct measurements of OH reactivity and then missing OH reactivity in a forest, missing OH reactivity has been reported for a wide range of environments by several research groups (Di Carlo et al., 2004; Yang et al., 2016). However, over time, there has been a general tendency for decreasing reported missing OH reactivity. This trend was anticipated even twenty years ago because the ability to measure larger, highly reactive molecules, such as sesquiterpenes, and oxygenated molecules has improving dramatically. With the fairly complete instrument suite on the DC-8, we would expect that the missing OH reactivity might be within the combined measurement and modeled uncertainty, which recently is typically ~30–40%, 90% confidence.

The median observed OH reactivity for land regions with NO less than 5 ppbv is 4.6 s^{-1} in the mixed layer and decreases to ~1 s^{-1} above ~3 km (Fig. 7). Over the ocean, the median value is 3.5 s^{-1} just above the surface and decreases to ~1 s^{-1} above 2 km. In the lowest 2 km, the median OH reactivity calculated with MCM is generally lower than the median observed OH reactivity over both land and ocean and the difference is the missing OH reactivity. The median missing OH reactivity is ~1.3 s^{-1} (30%) in the mixed layer over land and ~0.4 s^{-1} (12%) over ocean. The median OH reactivity over ocean for KORUS is almost twice that found in Atmospheric Tomography (ATom) over the tropical Pacific Ocean, but the missing OH reactivity in ATom was 0.5 s^{-1} about the same as for KORUS-AQ (Thames et al., 2020). Between 2 and 6 km, the missing OH reactivity becomes statistically insignificant. Thus, missing OH reactivity is confined to the PBL.

A map of the missing OH reactivity for all flights at altitudes below 2 km and for NO less than 5 ppbv shows substantial variability (Fig. 8).

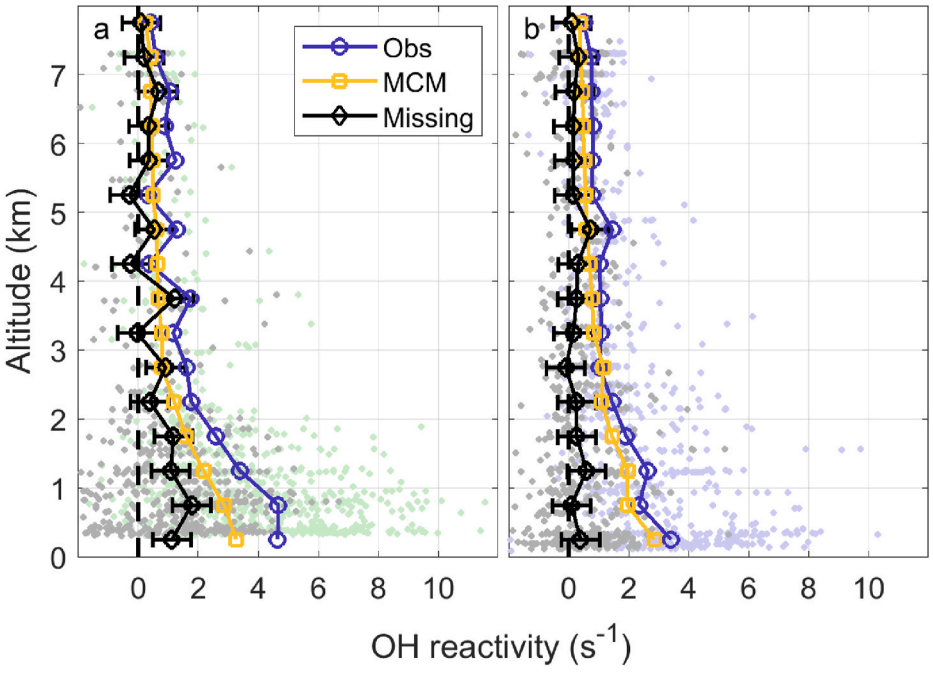

Fig. 7. Measured and model-calculated OH reactivity and missing OH reactivity as a function of altitude over land (a) and over ocean (b). Dots are individual 5-min observed OH reactivity over land (a, green) and ocean (b, blue); Gray dots are individual 5-min missing OH reactivity in both (a) and (b). Error bars are the measured OH absolute uncertainty (±0.64 s^{-1}, 95% confidence). Precision on individual 5-min averages is ±1.0 s^{-1}, 95% confidence. (For interpretation of the references to color in this figure legend, the reader is referred to the Web version of this article.)

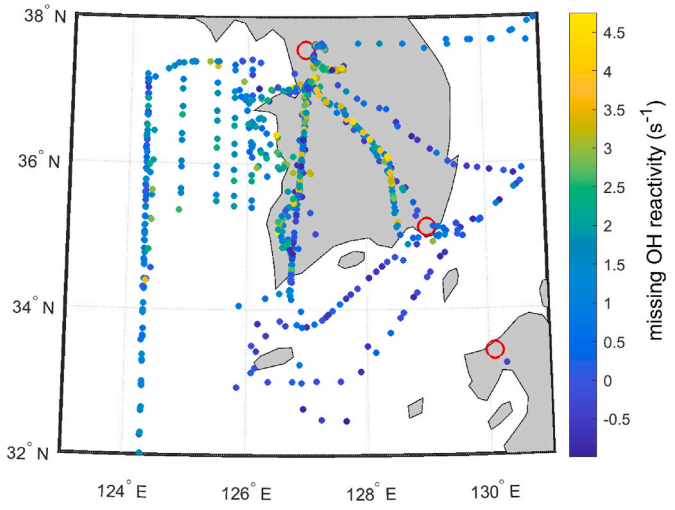

Fig. 8. Map of missing OH reactivity (5-min averages) at altitudes less than 2 km over South Korea and vicinity. The centers of Seoul, Busan, and Fukuoka, Japan are indicated by red circles, with Seoul to the north and Fukuoka to the south. (For interpretation of the references to color in this figure legend, the reader is referred to the Web version of this article.)

The greatest missing OH reactivity is in the SMA and along the flight corridors from Osan to Busan or Gwangji (126.7° longitude, 35.2° latitude) to the south of Osan. Over the East China Sea, the missing OH reactivity varies from 0 to ~2 s^{-1}, with a few exceptions. The near-zero missing OH reactivity occurs primarily over the ocean south of the South Korean peninsula, but can also be seen along flight tracks over the peninsula, including along the flight track from Osan to Gwangju. Factors other than location that are clearly important.

One important factor is season. KORUS-AQ occurred in the transition between winter and summer and during climatologically rising temperatures, which increased about 7 °C from the beginning to end of KORUS. As a result, missing OH reactivity roughly correlates with the day of the year, complicating the analysis of the spatial distribution of missing OH reactivity. For example, the flight along a straight line south through Gwangju was in early May and shows little to no missing OH reactivity. A repeat flight down the same flight corridor on 9 June had to deviate around controlled air space near 35° latitude and typically had 2-3 s^{-1} of missing OH reactivity.

Another important factor is wind direction. For example, on 10 June, the DC-8 flew at 8 km altitude directly to Fukuota, Japan, spiraled down, and then did mostly low-level legs to the west over the ocean before flying along the Osan-to-Gwangju flight corridor. Even though the low-level legs over this flight corridor were at the same time of day as the ones flown on 9 June, the missing OH reactivity on 10 June was 0–1.5 s^{-1}, substantially less than on 9 June. The temperature was a few degrees lower on 10 June, but the big difference was the wind direction. On 9 June, the wind was coming from the north to east, over the peninsula, but on 10 June, it was coming from south to west, over the ocean.

Thus, two important factors in determining the amount of missing OH reactivity appear to be the time of year and whether the air sampled was coming from over the ocean or over the Korean peninsula. The most missing OH reactivity was in air that was coming from South Korea itself. It is difficult to say if the source of missing OH reactivity is biogenic or anthropogenic, but, for some flights, enhanced missing OH reactivity seems to have spread from the SMA to nearby regions. The DC-8 instrument payload measured an extensive suite of both anthropogenic and biogenic VOCs, so a likely cause of the missing OH reactivity is a combination of oxygenated VOCs, perhaps ethanol and oxygenated products from C_{7+} aromatics, which were not quantitatively measured during KORUS-AQ but could be abundant in the SMA, and oxygenated biogenic VOS products. This combination can explain the seasonal increase and the land-based origin.

It may be that the missing OH reactivity affected the OH and HO_2 abundances as well as the O_3 production. However, the OH reactivity measurement is instantaneous, which means that it misses the subsequent reactions in the oxidation chemistry could be recycling OH and HO_2. For some VOCs, a substantial amount of HO_x is recycled, so that, without knowing the identity of the missing OH reactivity reactant, it is not possible to know if the missing OH reactivity is consistent with the observed OH and HO_2 and the calculated O_3 production.

3.4. Ozone production

How much O_3 increased during the day in the SMA was determined mainly by FO_3 due to the reactions of HO_2 and RO_2 with NO (Fig. 9), which, when the chemical loss DO_3 is subtracted, gives the net chemical O_3 production, PO_3. The calculated FO_3 using HO_2 that was observed and modeled by LaRC and MCM are shown as a function of the observed NO in the top panel and the calculated FO_3 using only RO_2 modeled by LaRC and MCM are shown in the lower panel of Fig. 8.

For HO_2, observed and modeled FO_3 agree up to NO of ~1 ppbv and increasingly diverge at greater NO (Fig. 9a). For 10 ppbv of NO, FO_3 using observed HO_2 is 3 times modeled and FO_3 calculated with LaRC HO_2 is 30% greater than that calculated with MCM. Above 10 ppbv, the difference grows much greater, but the number of data points is small. Some of this difference could be due to sampling from the DC-8 that, in 1 s, travels 100 m. Thus, it is possible that the DC-8 instruments sampled finer filaments of NO-rich air that was separated from the HO_2-rich background air, but each was recorded for that second (Olson et al., 2010). The resulting product of the two, averaged over a second, would be greater than the actual product in the atmosphere, giving an inflated calculated value for FO_3. The data points with NO above 10 ppbv were generally from missed approaches and so may have suffered from this problem. However, even if we eliminate all data from the missed approaches, the deviation of PO_3 calculated using observed HO_2 from that modeled is still evident for NO less than 10 ppbv.

The FO_3 from RO_2 calculated with LaRC is different from that

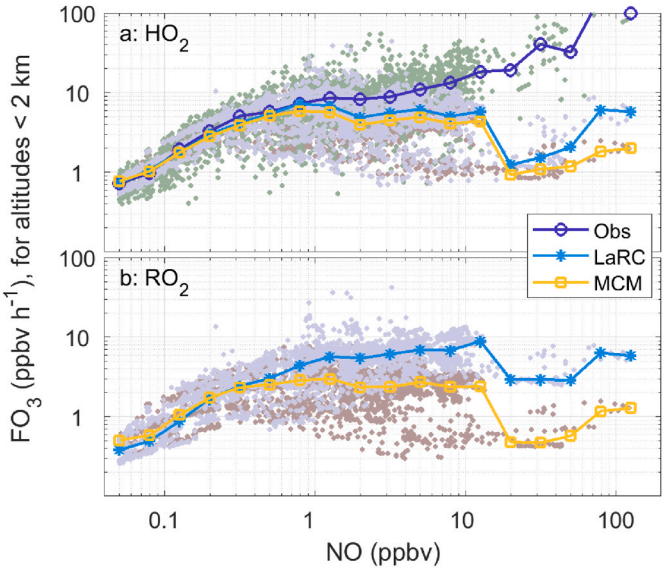

Fig. 9. FO_3 due to HO_2 (a) and to RO_2 (b) as a function on NO for measurements at altitudes below 2 km. Medians and 1-s data of PO_3 are shown for observed HO_2 (blue circles, green dots), LaRC modeled HO_2 (ligh blue stars and gray dots), and MCM modeled HO_2 (gold squares), as well as PO_3 from RO_2 modeled by LaRC (light blue stars and gray dots) and by MCM (gold squares and taupe dots). (For interpretation of the references to color in this figure legend, the reader is referred to the Web version of this article.)

calculated with the more explicit MCM (Fig. 9b). The difference begins at NO below 1 ppbv and then becomes a factor of 3 at 10 ppbv. At 10 ppbv, the difference in the FO_3 calculated with LaRC RO_2 is 6.5 ppbv h^{-1} greater than that calculated with MCM, which is only 1/3 of the difference between FO_3 calculated with observer HO_2 compared to that with modeled HO_2, 12 ppbv h^{-1}, but it still gives substantial uncertainty in total calculated FO_3 from both HO_2 and RO_2.

Although the FO_3 values may be inflated by the DC-8 passing through inhomogeneous air parcels during the missed approaches, the calculations still provide some insight into PO_3 in the SMA. The calculated PO_3 for LaRC, MCM, and observed HO_2 and LaRC and MCM RO_2 and the altitude-weighted average of the mixed layer and residual layer PO_3 are given in Table 1. The calculated PO_3 is greatest at midday for LaRC and MCM HO_2 and greatest early for observed HO_2. For the early missed approach the PO_3 calculated from observed HO_2 is 4–5 times larger than from LaRC, which is consistent with the differences in FO_3 at higher levels of NO in Fig. 8. The PO_3 differences using the modeled and observed HO_2 are smaller for the midday and late missed approaches. The differences between the LaRC and MCM PO_3 values are not due to FO_3 calculated from modeled HO_2, which are different by only 15%, but instead by the FO_3 calculated from modeled RO_2, for which MCM is only 40% of LaRC. Thus, the greatest uncertainty in the PO_3 calculation is due to the calculation of RO_2.

When PO_3 is adjusted by the altitude-weighted average of the mixed layer and residual layer values, the mean calculated values for the early missed approach drop and, in the case of the observed HO_2, drop by a factor of 5. As a result, the adjusted PO_3 becomes greatest in midday to late for all calculated values.

These results for PO_3 are somewhat different from the LaRC results presented in Schroeder et al. (2020), which are 3.2 ppbv h^{-1} for early, 8.1 ppbv h^{-1} for midday, and 7.5 ppbv h^{-1} for late. These values are all smaller than the values in Table 1. The main difference is that their early, midday, and late PO_3 values are calculated for all missed approaches, whereas we calculate them only for seven days that had three missed approaches. Our LaRC PO_3 values for midday and late are similar to theirs if we calculate them using all missed approaches. Another difference is that we calculate the averages over the mixed layer, and they calculate them over the lowest 1 km, which, in the early missed approach, included some PO_3 from the residual layer.

Using DC-8 observations from seven days that had early, midday, and late missed approaches, we can compare O_3 time-rate-of-change to the sum of all the terms on the right in eq. (1) by the procedure described in the Methods section. In Fig. 10, the comparison of the corrected time rate of change of O_x is compared to the calculated PO_3 using observed or modeled HO_2 and modeled RO_2 for morning and afternoon, both without and with simple O_3 heterogeneous chemistry. For the case without heterogeneous chemistry, typical values for the O_x rate of change are 4–9 ppbv h,[1] while in the afternoon, they are 6–14 ppbv h^{-1}. Using the PO_3 with observed HO_2 and MCM RO_2 agrees with the O_x rate of change best in the morning and PO_3 with LaRC HO_2 and RO_2 agrees best in the afternoon. PO_3 with MCM HO_2 and RO_2 is much lower than the O_x rate of change for both morning and afternoon. Given the uncertainties in the assumptions made, both PO_3 with observed HO_2 and LaRC HO_2 are consistent with the O_x rate of change, but PO_3 with MCM HO_2 is not.

When heterogeneous O_3 loss is included, with α equal 10^{-4}, the corrected O_x rate of change shifts to 5–15 ppbv h^{-1} for morning and 7–17 ppbv h^{-1} in the afternoon, shifts of 1–6 ppbv h^{-1}. For the morning, the corrected O_x rate of change is now larger than all the calculated PO_3 values and, for the afternoon, is larger than all but on a few days. This comparison indicates that the likely α for heterogeneous losses is less than 10^{-4}, although it could be a few times 10^{-5} and still be consistent with the PO_3 values calculated from observations and LaRC.

PO_3 and $\Delta O_x/\Delta t$ shown in Fig. 10 were averaged and compared to the results of Schroeder et al. (2020) in Table 2. The LaRC PO_3 is similar to that in Schroeder et al., as would be expected. However, the average $\Delta O_x/\Delta t$ from this work is almost twice as large as that from Schroeder et al.. This difference is primarily due to the correction of the earlier O_x value for known loss before subtracting it from the later O_3 and dividing by the time interval for both morning and afternoon. The resulting $\Delta O_x/\Delta t$ is most consistent with the PO_3 calculated with the observed HO_2 and the LaRC RO_2.

As mentioned in Schroeder et al. (2020), Seoul Air Base is in the strongest O_x source region and, during the afternoon, advection could bring air with a little less O_3 from the East China Sea over the site. Thus, $\Delta O_x/\Delta t$ from PO_3 could actually be even greater than given in Table 2. However, as mention previously, the uncertainty in this simple analysis are large, but probably not much larger than the uncertainty in the O_x calculated by chemical transport models for Seoul Air Base or any other single location.

Table 1
Mean values of calculated PO_3 for missed approaches.

Time \ PO_3 (ppbv h^{-1})	LaRC HO_2 and RO_2	MCM HO_2 and RO_2	Obs HO_2; LaRC RO_2	Obs HO_2; MCM RO_2
early	4.9	1.3	24.4	22.7
midday	9.9	5.4	14.1	11.7
late	9.1	4.8	11.4	7.0
Altitude-weighted average of the mixed layer and residual layer PO_3				
early	1.7	1.0	4.9	4.1
midday	7.4	4.7	9.9	7.9
late	9.1	4.8	11.4	7.0

Table 1. Mean values for calculated PO_3 for seven days with three missed approaches.

Table 2
Mean values of morning and afternoon PO_3 and $\Delta O_x/\Delta t$.

	This work					Schroeder et al. (2020)	
Time \ PO_3 (ppbv h^{-1})	LaRC	MCM	Obs/ LaRC	Obs/ MCM	$\Delta O_x/\Delta t$	PO_3	$\Delta O_x/\Delta t$
morning	4.7	2.8	7.3	5.7	**6.4**	5.7	4.8
afternoon	8.2	4.8	10.6	7.3	**10.5**	7.8	4.6

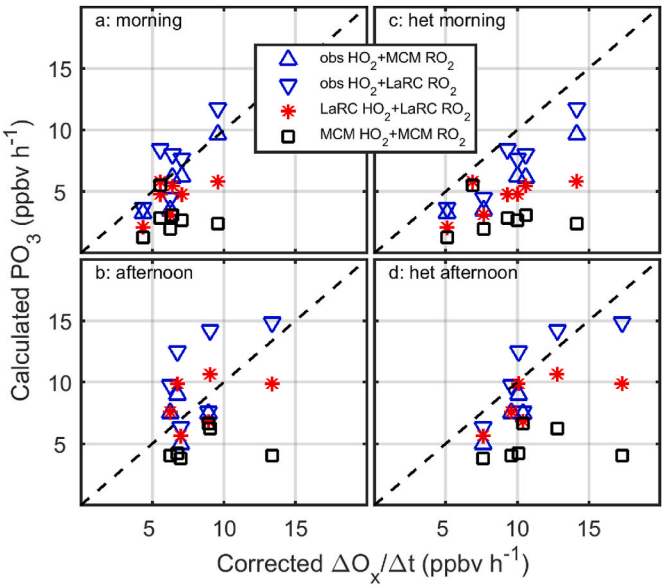

Fig. 10. Observed change in O_x between morning and noon at the Seoul Airport, corrected for difference in the MLH at the two times versus the calculated net PO_3 from observed and modeled HO_2 and modeled RO_2 from the two models.

4. Conclusions

The comparison of measured, LaRC, and MCM OH and HO_2 shares characteristics observed in several previous airborne studies: some deviations with altitude approaching statistical significance; scatter plots with slopes within uncertainties of 1.0 and percent differences within 20% of 0; and lower R^2 correlations indicating considerable point-to-point scatter. For instance, it is not possible to say from these data that the explicit MCM chemistry is a better representation of atmospheric chemistry than the lumped VOC LaRC mechanism. Both appear to be able to simulate OH and HO_2 to within the combined measurement and model uncertainties, but only when heterogeneous HO_2 uptake is not included in the model.

The scatter in the comparisons is not unexpected for several reasons: the likely heterogeneity of the chemical composition, especially in the planetary boundary layer, so that the measurements with sampling intervals greater than a few seconds cannot capture this heterogeneity; the interpolations required to convert measurements made on different time scales to 1-s time steps for LaRC or 1-min time steps for MCM; and likely variability in instrument performance and calibrations.

This work demonstrates that observations of OH and HO_2 provide valuable tests of the ability of photochemical models to correctly represent oxidation chemistry, particularly for environments with the levels of pollution encountered during KORUS-AQ. Here we have compared observed OH and HO_2 to photochemical box models. However, observed OH and HO_2 should also be used to test the chemical transport models that influence the advice given to policy makers about ozone and particle pollution mitigation strategies.

Data availability

Data and LaRC model output are openly available from the NASA Langley Research Center archive: KORUS-AQ DOI: 10.5067/Suborbital/KORUSAQ/DATA01 (Aknan and Chen, 2017).

CRediT authorship contribution statement

William H. Brune: Investigation, Methodology, Writing – original draft, review & editing, Software, Data curation, Formal analysis, Project administration, Supervision; **David O. Miller:** Investigation, Methodology, Writing - review & editing, Software, Data curation. **Alexander B. Thames:** Writing - review & editing, Investigation, Data curation. **Alexandra L. Brosius:** Investigation, Data Curation, Methodology, Software, Formal analysis. **Donald R. Blake:** Investigation, Data Curation. **Nicola J. Blake:** Investigation, Data Curation. **Gao Chen:** Investigation, Data Curation. **James H. Crawford:** Investigation, Methodology, Data Curation. **Joshua P. Digangi:** Investigation, Data Curation. **Glenn Diskin:** Investigation, Data Curation. **Alan Fried:** Investigation, Data Curation. **Samuel R. Hall:** Writing - review & editing, Investigation, Data Curation. **Thomas F. Hanisco:** Investigation, Data Curation. **Greg L. Huey:** Investigation, Data Curation. **Stacey C. Hughes:** Investigation, Data Curation. **Michelle Kim:** Investigation, Data Curation. **Simone Meinardi:** Investigation, Data Curation. **Denise D. Montzka:** Investigation, Data Curation. **Sally E. Pusede:** Investigation, Data Curation. **Jason R. Schroeder:** Investigation, Data Curation. **David J. Tanner:** Investigation, Data Curation. **Alex Teng:** Investigation, Data Curation. **Kirk Ullmann:** Investigation, Data Curation. **James Walega:** Investigation, Data Curation. **Andrew Weinheimer:** Investigation, Data Curation. **Armin Wisthaler:** Investigation, Data Curation. **Paul O. Wennberg:** Investigation, Data Curation.

Declaration of competing interest

The authors declare that they have no known competing financial interests or personal relationships that could have appeared to influence the work reported in this paper.

Acknowledgments

We thank our fellow KORUS_AQ scientists from the United States and Korea, Barry Lefer and the rest of NASA management involved in KORUS-AQ, and the NASA DC-8 pilots and operations crew. VOC measurements by PTR-MS were supported by the Austrian Federal Ministry for Transport, Innovation and Technology (bmvit) through the Austrian Space Applications Programme (ASAP) of the Austrian Research Promotion Agency (FFG). The PTR-MS instrument team (P. Eichler, L. Kaser, T. Mikoviny, M. Müller) is acknowledged for providing the PTR-MS data for this study. SRH and KU were supported by NASA grant NNX15AT99G. WHB, DOM, ABT, and ALB were supported by NASA grants NNX15AT82G and 80NSSC19K1590.

References

Aknan, A., Chen, G., 2017. NASA LaRC Airborne Science Data for Atmospheric Composition – KORUS-AQ. https://doi.org/10.5067/Suborbital/KORUSAQ/DATA01.

Abbatt, J.P.D., Lee, A.K.Y., Thornton, J.A., 2012. Quantifying trace gas uptake to tropospheric aerosol: recent advances and remaining challenges. Chem. Soc. Rev. 41, 6555–6581. https://doi.org/10.1039/C2CS35052A.

Appel, K.W., Gilliland, A.B., Sarwar, G., Gilliam, R.C., 2007. Evaluation of the community multiscale Air quality (CMAQ) model version 4.5: sensitivities impacting model performance: Part I: ozone, atmos. Environ. Times 41, 9603–9615. https://doi.org/10.1016/j.atmosenv.2007.08.044.

Brune, W.H., Baier, B.C., Thomas, J., Ren, X., Cohen, R.C., Pusede, S.E., Browne, E.C., Goldstein, A.H., Gentner, D.R., Keutsch, F.N., Thornton, J.A., Harrold, S., Lopez-Hilfiker, F.D., Wennberg, P.O., 2016. Ozone production chemistry in the presence of urban plumes. Faraday Discuss 189, 169–189.

Brune, W.H., Ren, X.R., Zhang, L., Mao, J., Miller, D.O., et al., 2018. Atmospheric oxidation in the presence of clouds during the Deep convective Clouds and chemistry (DC3) study. Atmos. Chem. Phys. 18, 14493–14510.

Brune, W.H., Miller, D.O., Thames, A.B., Allen, H.M., Apel, E.C., Blake, D.R., et al., 2020. Exploring oxidation in the remote free troposphere: insights from Atmospheric Tomography (ATom). J. Geophys. Res. Atmos. 125, e2019JD031685 https://doi.org/10.1029/2019JD031685.

Chen, S., Brune, W.H., 2012. Global sensitivity analysis of ozone production and O3-NOx-VOC limitation based on field data. Atmos. Environ. 55, 288–296. https://doi.org/10.1016/j.atmosenv.2012.03.061.

Chen, S., Brune, W.H., Oluwole, O.O., Kolb, C.E., Bacon, F., Li, G.Y., Rabitz, H., 2012. Global sensitivity analysis of the regional atmospheric chemical mechanism: an application of random sampling-high dimensional model representation to urban oxidation chemistry. Environ. Sci. Technol. 46, 11162–11170. https://doi.org/10.1021/es301565w.

Christian, K.E., Brune, W.H., Mao, J., 2017. Global sensitivity analysis of the GEOS-Chem chemical transport model: ozone and hydrogen oxides during ARCTAS. Atmos. Chem. Phys. 17, 3769–3784. https://doi.org/10.5194/acp-17-3769-2017.

Crawford, J., Davis, D., Olson, J., Chen, G., Liu, S., Gregory, G., Blake, D., 1999. Assessment of upper tropospheric HO_x sources over the tropical Pacific based on NASA GTE/PEM data: net effect on HO_x and other photochemical parameters. J. Geophys. Res. Atmos. 104 (D13), 16255–16273. https://doi.org/10.1029/1999JD900106.

Crawford, J.H., Ahn, J.Y., Al-Saadi, J., Chang, L., Emmons, L.K., Kim, J., Lee, G., Park, J. H., Park, R.J., Woo, J.H., 7, Chang-Keun Song, C.-K., Hong, J.-H., Hong, Y.-.D., Lefer, B.L., Lee, M., Lee, T., Kim, S., Min, K.-E., Yum, S.S., Shin, H.J., Kim, Y.-W., Choi, J.-S., Park, J.-S., Szykman, J.J., Long, R.W., Jordan, C.E., Simpson, I.J., Fried, A., Dibb, J.E., Cho, S.Y., Kim, Y.P., 2021. The Korea–United States air quality (KORUS-AQ) field study. Elem Sci Anth 9. https://doi.org/10.1525/elementa.2020.00163.

Di Carlo, P., Brune, W.H., Martinez, M., Harder, H., Lesher, R., Ren, X.R., Thornberry, T., Carroll, M.A., Young, V., Shepson, P.B., Riemer, D., Apel, E., Campbell, C., 2004. Missing OH reactivity in a forest: evidence for unknown reactive biogenic VOCs. Science 304, 722–725.

de Foy, B., Brune, W.H., Schauer, J.J., 2020. Changes in ozone photochemical regime in Fresno, California from 1004 to 2018 deduced from changes in the weekend effect. Eviron. Pollution 263, 114380. https://doi.org/10.1016/j.envpol.2020.114380.

Faloona, I.C., Tan, D., Lesher, R.L., Hazen, N.L., Frame, C.L., Simpas, J.B., Harder, H., Martinez, M., Di Carlo, P., Ren, X.R., Brune, W.H., 2004. A laser-induced fluorescence instrument for detecting tropospheric OH and HO_2: characteristics and calibration. J. Atmos. Chem. 47, 139–167.

Feiner, P.A., Brune, W.H., Miller, D.O., Zhang, L., Cohen, R.C., Romer, P.S., Goldstein, A. H., Keutsch, F.N., Skog, K.M., Wennberg, P.O., Nguyen, T.B., Teng, A.P., DeGouw, J., Koss, A., Wild, R.J., Brown, S.S., Guenther, A., Edgerton, E., Baumann, K., Fry, J.L., 2016. Testing atmospheric oxidation in an Alabama forest. J. Atmos. Sci. 73 (12), 4699–4710.

Fuchs, H., Bohn, B., Hofzumahaus, A., Holland, F., Lu, K.D., Nehr, S., Rohrer, F., Wahner, A., 2011. Detection of HO_2 by laser-induced fluorescence: calibration and interferences from RO_2 radicals. Atmos. Meas. Tech. 4, 1209–1225.

Fittschen, C., Assaf, E., Vereecken, L., 2017. Experimental and theoretical investigation of the reaction NO+OH+O2 → HO2+NO2. J. Phys. Chem. 121, 4652–4657. https://doi.org/10.1021/acs.jpca.7b02499.

Harley, R.A., Marr, L.C., Lehner, J.K., Giddings, S.N., 2005. Changes in motor vehicle emissions on diurnal to decadal time scales and effects on atmospheric composition. Environ. Sci. Technol. 39 (14), 5356e5362.

Im, U., Bianconi, R., Solazzo, E., Kioutsioukis, I., Badia, A., Balzarini, A., Baró, R., Bellasio, R., Brunner, D., Chemel, C., Curci, G., Flemming, J., Forkel, R., Giordano, L., Jiménez-Guerrero, P., Hirtl, M., Honzak, L., Jorba, O., Knote, C., Kuenen, J.J.P., Makar, P.A., Manders-Groot, A., Neal, L., Pérez, J.L., Pirovano, G., Pouliot, G., San Jose, R., Savage, N., Schroder, W., Sokhi, R.S., Syrakov, D., Torian, A., Tuccella, P., Werhahn, J., Wolke, R., Yahya, K., Zabkar, R., Zhang, Y., Zhang, J., Hogrefe, C., Galmarini, S., 2015. Evaluation of operational on-line-coupled regional air quality models over Europe and North America in the context of AQMEII phase 2. Part I: ozone, Atmos. Environ. Times 115, 404–420.

IQAir,2021 https://www.iqair.com/us/south-korea/seoul, accessed 05/06/2021.

Jenkin, M.E., Saunders, S.M., Wagner, V., Pilling, M.J., 2003. Protocol for the development of the Master Chemical Mechanism, MCM v3 (Part B): tropospheric degradation of aromatic volatile organic compounds. Atmos. Chem. Phys. 3 (1), 181–193. https://doi.org/10.5194/acp-3-181-2003.

Jung, H.C., Moon, B.K., Wie, J., 2018. Seasonal changes in surface ozone over South Korea. Heliyon 4, e00515. https://doi.org/10.1016/j.heliyon.2018.e00515.

Kang, Yoon-Hee, Oh, Inbo, Jeong, Ju-Hee, Bang, Jin-Hee, Kim, Yoo-Keun, Kim, Soontae, Kim, Eunhye, Hong, Ji-Hyung, Lee, Dae-Gyun, 2016. Comparison of CMAQ ozone simulations with two chemical mechanisms (SAPRC99 and CB05) in the Seoul Metropolitan region. J. Environ. Sci. Int. 25 (1), 85–97. https://doi.org/10.5322/JESI.2016.25.1.85.

Kim, Y., Lee, G., 2018. Trend of air quality in Seoul: policy and science. Aerosol Air Qual. Res. 18 https://doi.org/10.4209/aaqr.2018.03.0081.

Kovacs, T., Brune, W.H., 2001. Total OH loss rate measurement. J. Atmos. Chem. 39, 105–122.

Le, T., Wang, Y., Liu, J., Yang, J., Yung, Y.K., Li, G., Seinfeld, J.H., 2020. Unexpected air pollution with marked emission reductions during the COVID-19 outbreak in China. Science 369, 702–706. https://doi.org/10.1126/science.abb7431.

Li, K., Jacob, D.J., Liao, H., Shen, L., Zhang, Q., Bates, K.H., 2018. Anthropogenic rivers of the 2013-2017 trens in summer surface ozone in China. Proc. Natl. Acad. Sci. U.S. A. https://doi.org/10.1073/pnas.1812168116.

Mao, J., Ren, X., Brune, W.H., Olson, J.R., Crawford, J.H., Fried, A., Huey, L.G., Cohen, R.C., Heikes, B., Singh, H.B., Blake, D.R., Sachse, G.W., Diskin, G.S., Hall, S. R., Shetter, R.E., 2009. Airborne measurement of OH reactivity during INTEX-B. Atmos. Chem. Phys. 9, 163–173.

Mao, J., Fan, S., Jacob, D.J., Travis, K.R., 2013. Radical loss in the atmosphere from Cu-Fe redox coupling in aerosols. Atmos. Chem. Phys. 13, 509–519.

Miller, D.O., Brune, W.H., 2021. Investigating the understanding of oxidation chemistry using 20 Years of airborne OH and HO_2 observations. submitted to J. Geophys. Res.

Nault, B.A., Campuzano-Jost, P., Day, D.A., Schroder, J.S., Anderson, B., Beyersdorf, A.J., Blake, D.R., Brune, W.H., Choi, Y., Corr, C.A., de Gouw, J.A., Dibb, J., DiGangi, J.P., Diskin, G.S., Fried, A., Huey, L.G., Kim, M.J., Knote, C.J., Lamb, K.D., Lee, T., Park, T., Pusede, S.E., Scheuer, E., Thornhill, K.L., Woo, J.-H., Jimenez, J.J., 2018. Secondary organic aerosol production from local emissions dominates the organic aerosol budget over Seoul, South Korea, during KORUS-AQ. Atmos. Chem. Phys. 18, 17769–17800. https://doi.org/10.5194/acp-18-17769-2018.

Oak, Y.J., Park, R.J., Schroeder, J.R., Crawford, J.H., Blake, D.R., Weinheimer, A.J., Woo, J.-H., Kim, S.-W., Yeo, H., Fried, A., Wisthaler, A., Brune, W.H., 2019. Evaluation of simulated O_3 production efficiency during the KORUS-AQ campaign: implications for anthropogenic NO_x emissions in Korea. Elementa-Sci. Anthropocene 7, 56. https://doi.org/10.1525/elementa.394.

Olson, J.R., Crawford, J.H., Chen, G., Fried, A., Evans, M.J., Jordan, C.E., Tan, D., 2004. Testing fast photochemical theory during TRACE-P based on measurements of OH, HO_2 and CH_2O. J. Geophys. Res. Atmos. 109 (15), 1–16. https://doi.org/10.1029/2003JD004278.

Olson, J.R., Crawford, J.H., Chen, G., Brune, W.H., Faloona, I.C., Tan, D., Martinez, M., 2006. A reevaluation of airborne HO_x observations from NASA field campaigns. J. Geophys. Res. Atmos. 111, 1–12. https://doi.org/10.1029/2005JD006617.

Park, R.J., Hong, S.K., Kwon, H.-A., Kim, S., Guenther, A., Woo, J.H., Loughner, C.P., 2014. An evaluations of ozone dry deposition simulations in East Asia. Atmos. Chem. Phys. 14, 7929–7940. https://doi.org/10.5194/acp-14-7929-2014.

Park, R.J., Oak, Y.J., x Emmons, L.K., Kim, C.-H., Pfister, G.G., Carmichael, G.R., Saide5, P.E., Cho, S.-Y., Kim, S., Woo, J.-H., Crawford, J.H., Gaubert, B., Lee, H.J., Park, S.-Y., Jo, Y.-J., Gao, M., Tang, B., Stanier, C.O., Shin, S.S., Park, H.Y., Bae, C., Kim, E., 2021. Multi-model intercomparisons of air quality simulations for the KORUS-AQ campaign. Elem Sci Anth 9, 1. https://doi.org/10.1525/elementa.2021.00139.

Pollack, I.B., Ryerson, T.B., Trainer, M., Neuman, J., Roberts, J.M., Parrish, D.D., 2013. Trends in ozone, its precursors, and related secondary oxidation products in Los Angeles, California: a synthesis of measurements from 1960 to 2010. J. Geophys. Res. Atmos. 118 (11), 5893e5911.

Reuters, 2021 https://www.reuters.com/article/idUSL3N15U0M2 , accessed 05/06/2021.

Saunders, S.M., Jenkin, M.E., Derwent, R.G., Pilling, M.J., 2003. Protocol for the development of the Master Chemical Mechanism, MCMv3 (Part A): tropospheric degradation of non-aromatic volatile organic compounds. Atmos. Chem. Phys. 3 (1), 161–180. https://doi.org/10.5194/acp-3-161-2003.

Schroeder, J.R., Crawford, J.H., Ahn, J.Y., Chang, L., Fried, A., Walega, J., Weinheimer, A., Montzka‖, D.D., Hall, S.R., Ullmann, K., Wisthaler, A., Mikoviny, T., Chen, G., Blake, D.R., Blake, N.J., Hughes, S.C., Meinardi, S., Diskin, G., Digangi, J. P., Choi, Y., Pusede, S.E., Huey, G.L., Tanner, D.J., Kim, M., Wennberg, P.O., 2020. Observation-based modeling of ozone chemistry in the Seoul metropolitan area during the Korea-United States air quality study (KORUS-AQ). Elem Sci Anth 8, 3. https://doi.org/10.1525/elementa.400.

Susaya, J., Kim, K.-H., Shon, Z.-H., Brown, R.J.C., 2013. Demonstration of long-term increases in tropospheric O_3 levels: causes and potential impacts. Chemosphere 92, 1520–1528. https://doi.org/10.1016/j.chemosphere.2013.04.017.

Thames, A.B., Brune, W.H., Miller, D.O., Allen, H.M., Apel, E.C., Blake, D.R., Bui, T.P., Commane, R., Crounse, J.D., Daube, B.C., Diskin, G.S., DiGangi, J.P., Elkins, J.W., Hall, S.R., Hanisco, T.F., Hannun, R.A., Hintsa, E., Hornbrook, R.S., Kim, M.J., McKain, K., Moore, F.L., Nicely, J.M., Peischl, J., Ryerson, T.B., St Clair, J.M., Sweeney, C., Teng, A., Thompson, C.R., Ullmann, K., Wennberg, P.O., Wolfe, G.M., 2020. Missing OH reactivity in the global marine boundary layer. Atmos. Chem. Phys. 20, 4013–4029. https://doi.org/10.5194/acp-20-4013-2020.

Thompson, C.R., et al., 2021. The NASA atmospheric Tomography (ATom) mission: imaging the chemistry of the global atmosphere. submitted to Bull. Am. Met. Soc.

Wolfe, G.M., Marvin, M.R., Roberts, S.J., Travis, K.R., Liao, J., 2016. The framework for 0-D atmospheric modeling (F0AM) v3.1. Geosci. Model Dev. (GMD) 9 (9), 3309–3319. https://doi.org/10.5194/gmd-9-3309-2016.

Wolfe, G.M., 2017. F0AM box model. available at: https://sites.google.com/site/wolfegm/models.

Yang, Y., Shao, M., Wang, X., Noelscher, A.C., Kessel, S., Guenther, A., Williams, J., 2016. Towards a quantitative understanding of total OH reactivity: a review. Atmos. Environ. 134, 147–161. https://doi.org/10.1016/j.atmosenv.2016.03.010.

York, D., Evensen, N.M., Martınez, M.L., De Basabe Delgado, J., 2004. Unified equations for the slope, intercept, and standard errors of the best straight line. Am. J. Phys. 72 (3), 367–375. https://doi.org/10.1119/1.1632486.